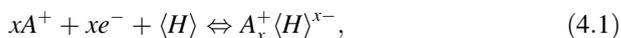


Chapter 4

Reliability of the Rigid-Band Model in Lithium Intercalation Compounds

4.1 Introduction

Layered compounds, in particular the transition-metal dichalcogenides (TMDs) and transition-metal oxides (TMOs), can be intercalated with a wide range of both organic and inorganic materials which may have a profound influence on the physical properties of the host compound [1]. The intercalation reaction in these compounds is driven by charge transfer from the intercalant to the host layered compound conduction band and thus electron-donating species can take place in such a reaction. The reversible ion-electron transfer reaction is classically represented by the scheme:



in the usual case where $\langle H \rangle$ is the host material, A an alkali metal and x the molar intercalation fraction. The electronic transport plays an important role in such reaction toward the formation of intercalation compounds. It also governs the phase transitions as the parameter expansion of the host structure has an electronic component. Consequently, it is possible to consider three classes of intercalation reaction that correspond to the different steps in the delocalization of the transferred electrons. The level of acceptance can be either a discrete atomic state, or a molecular level of a discrete polyatomic entity existing in the structure, or part of a conduction band.

In this chapter, we present the physical properties of cathodes materials and verify the applicability of the rigid-band model for intercalation compounds with a layered structure namely transition-metal chalcogenides MX_2 ($M = \text{Ti, Ta, Mo, W}$; $X = \text{S, Se}$) and oxides LiMO_2 ($M = \text{Co, Ni}$) as well. Electrical and optical properties are investigated. For some materials, we observe different degrees of irreversibility in the intercalation process and lattice evolution to the complete destruction of the host. Since the purpose here is the study of the materials in the framework of

materials science, all the electrochemical properties reported in this chapter have been recorded at low rate $C/12$ or $C/24$ to be close to thermodynamic equilibrium so that they can be related to the physical properties.

4.2 Evolution of the Fermi Level

Let consider the schematic representation of Fig. 4.1 providing an easy way to visualize the energetic levels of the three active components of a lithium battery that are the negative and positive electrodes and the electrolyte. Taking into account the description of physicists, the vacuum refers the zero-energy level. The electronic band structure of a material is characterized by three energies: the work function W that is the minimum thermodynamic energy to remove an electron from the Fermi level of a solid to the vacuum $W = E_{\text{vac}} - E_F$, the electron affinity $E_{\text{EA}} = E_{\text{vac}} - E_{\text{cb}}$ that is the energy obtained by moving an electron from the bottom of the conduction band to the vacuum and the band gap $E_g = E_{\text{vb}} - E_{\text{cb}}$ is the energy separation between the valence band E_{vb} and the conduction band E_{cb} . The negative electrode is lithium metal, which is an infinite reservoir of electrons; so electrons in a metal can be viewed as free electrons in a conduction band with $W_{(\text{Li})} = E_{\text{EA}(\text{Li})} \approx 1.5$ eV. The electrolyte is an electronic insulating medium characterized by a wide band gap $E_g > 4$ eV, which is the separation between the occupied and unoccupied molecular orbital energies that are HOMO and LUMO level, respectively. The case of the positive electrode is more complex as it is a semiconductor with various locations for the Fermi level that is not necessarily at the position $E_F = (E_{\text{cb}} + E_{\text{vb}})/2$. For instance, TiS_2 is a degenerate semiconductor with $E_g \approx 0.2$ eV [2], while LiCoO_2 is a p-type semiconductor with $E_g \approx 2.4$ eV and $W = 4.36$ eV that makes the Fermi level 0.4 eV above the top of the valence band [3].

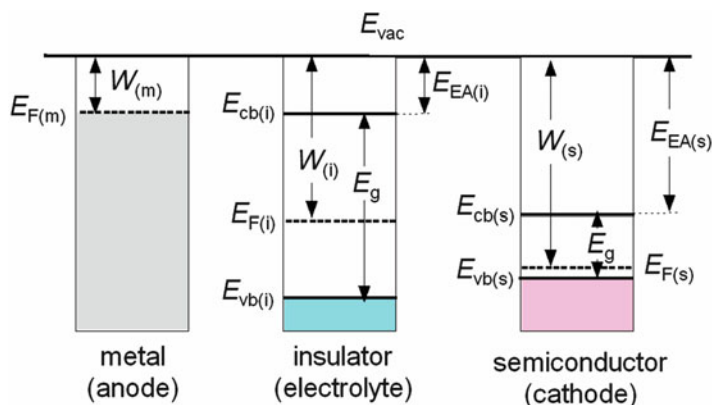


Fig. 4.1 Schematic representation of the electronic structure of the active elements of a lithium battery. E_{EA} indicates the electron affinity, W represents the work function and E_g is the band gap energy of the materials

The rigid-band model (RBM) is a useful approximation for describing the changes in electronic properties of the host material with intercalation. Sellmyer [4] distinguishes two versions of the rigid-band model for dilute solid solutions, which might be called the electron-gas RBM and the screened-impurity RBM. In the former, described mainly by Jones [5], the valence electrons are regarded essentially as in plane wave states and the only effect of alloying with an element having a valence difference ΔZ , is to change the free electron density to a new value, that obtained simply by scaling the valences of the solvent and solute according to their atomic fractions in the alloy. In this case, the Fermi energy in the material has changed accordingly, but E_{BC} remains unchanged. In the screened-impurity RBM of Friedel [6], it is recognized that the electron gas cannot support an electric field at long distances from the charge impurity. The reason is that the conduction electrons will redistribute themselves to screen out the Coulomb field, an effect that is measured by the dielectric constant, which is large in conducting materials. In this case, any charged impurity added to a solid will polarize the solid, which generates a Coulomb potential. Therefore, the Fermi energy is unchanged, but the whole conduction band has been shifted by this potential (Fig. 4.2).

The concept of rigid-bands implies chemical stability of the system. From the energetic point of view, this means the total energy of the substance is little affected by the addition of intercalated electrons. The consequence is that the structure too is stable, and the only energy band involved in intercalation is the narrow d -conduction band in TMDs. These are precisely the properties most desirable in a good cathode material, which provide features such as stable voltage against aging and mechanical durability [1]. It is most important, therefore, to investigate theoretically and experimentally how well the approximation can apply in a system employed for the lithium battery cathode.

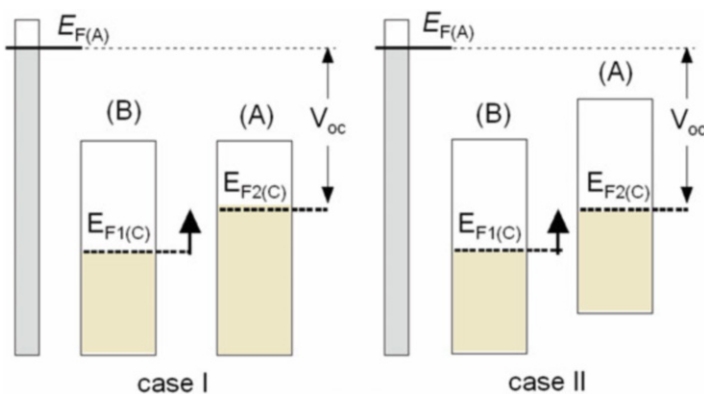


Fig. 4.2 Scheme of the Fermi level evolution in the frame of the rigid-band model (RBM). Two situations are considered: case I represents the electron-gas RBM, case II shows the screened-impurity RBM. (B) and (A) mean before and after lithium insertion, respectively. In both cases, the cell voltage V_{oc} is the same

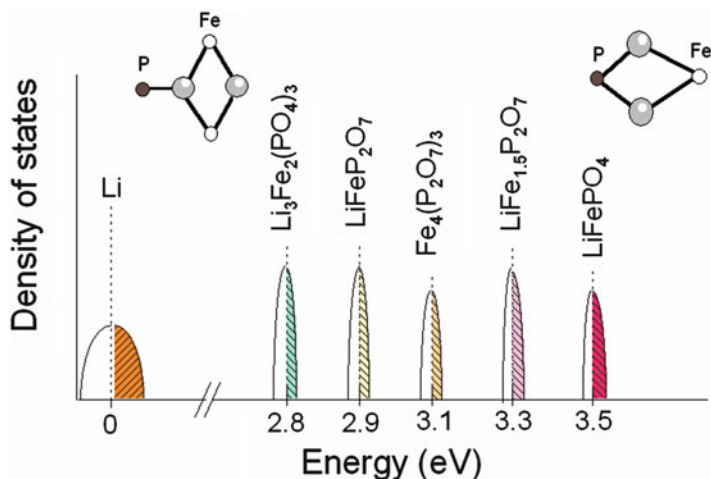


Fig. 4.3 Position of the iron redox energies to the Li^0/Li^+ in various Fe-containing lithium insertion hosts and consequent changes in cell voltages, illustrating the role of polyanions

As the potential of an insertion compound-based lithium battery is determined by the difference between the chemical potentials of electrodes (Eq. 1.6), the crystal chemistry of the cathode governs the cell voltage. As an example, Fig. 4.3 illustrates the role of the polyanions, i.e., $(\text{PO}_4)^{3-}$ and $(\text{P}_2\text{O}_7)^{4-}$, in iron-containing lithium insertion compounds, for which positions of the iron redox energies relative to Li^0/Li^+ changes as a function of the cation environment. This phenomenon has been described as the inductive effect by Goodenough [7]. It depends on the framework connectivity. For instance, the fluorophosphate compounds are expected to exhibit a high cell potential as a result of both the inductive effect of $(\text{PO}_4)^{3-}$ group and the electron-withdrawing character of the F^- ion.

4.3 Electronic Structure of TMDs

Considerations of the structural and chemical similarities in the layer structure of TMDs led Wilson and Yoffe [8–10] to suggest that the electronic energy band structures of the materials might also be similar and that the range of observed optical and electrical properties results from differences in the filling of band subgroups as the number of valence electrons is changed. While a completely rigid band model of the TMD compounds cannot account for all properties, theoretical calculations and experiments show that the basic view of the materials is probably correct: the character and the order of the various band subgroups remain the same, while their separations and widths vary slightly with changes in the constituents and the type of coordination unit in the crystal structure.

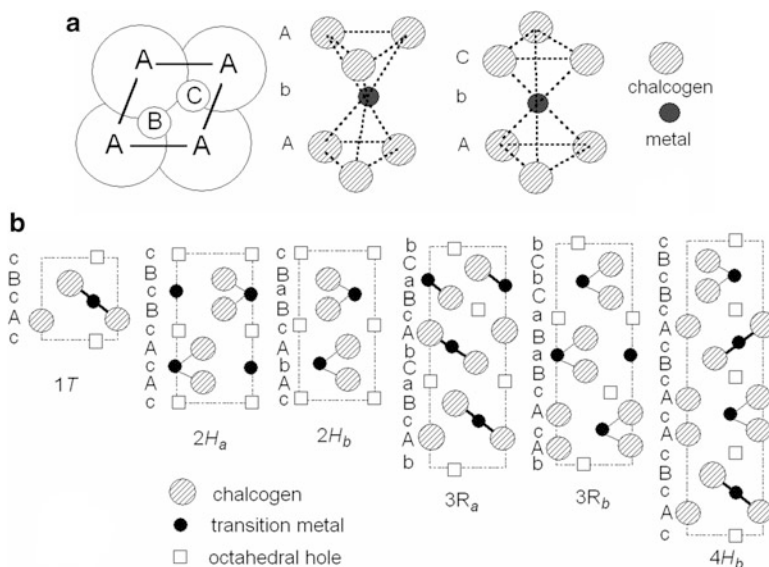


Fig. 4.4 (a) The octahedral and trigonal prismatic structures of MX_2 compounds. A, B, C represent the three nonequivalent positions for a close-packed stacking. In octahedron and tetrahedron, capital letters denote the chalcogen atoms and lower case letters the metal atoms. (b) Elementary unit cell of simple polytypes of TMDs in the $\langle 1120 \rangle$ projection

TMDs have a layered structure made up of a sheet of metal atoms M sandwiched between two sheets of chalcogen atoms X (Fig. 4.4). The $X-M-X$ layers are held together by weak van der Waals forces. Each sheet consists of atoms in a hexagonally close-packed network as shown in Fig. 4.4a. This structure allows almost unlimited expansion of the interslab distance upon insertion of electron-donating species in the layer. Although initial interest in these intercalation compounds was driven by their superconducting properties (at very low temperature), these were used as the active electrode of secondary lithium batteries [8]. Three nonequivalent hexagonally close-packed positions are noted A, B , and C . Two types of coordination structure are possible, either one or both can form the basic unit of the crystal. In the trigonal prismatic coordination, the sandwich of $X-M-X$ follows the AbA sequence and in the octahedral coordination it follows the AbC sequence (Fig. 4.4a). Capital letters denote the chalcogen atoms and lower case letters the metal atoms.

A rational nomenclature adopted for naming the different polymorphs and polytypes proposed Brown and Beerntsen [11] is presented in Fig. 4.4b. In designating the polytypes, one first indicates the number of sandwiches required to obtain a unit cell perpendicular to the plane of the layers, then the overall symmetry of the structure: trigonal T, hexagonal H, or rhombohedral R. Lower case subscripts are used to distinguish polytype otherwise similarly labeled, e.g., 2H_a and 2H_b. Thus the simplest polytype with octahedral coordination, labeled 1T, has a repeat of the sandwich perpendicular to the layer, i.e., this polytype is obtained by piling the

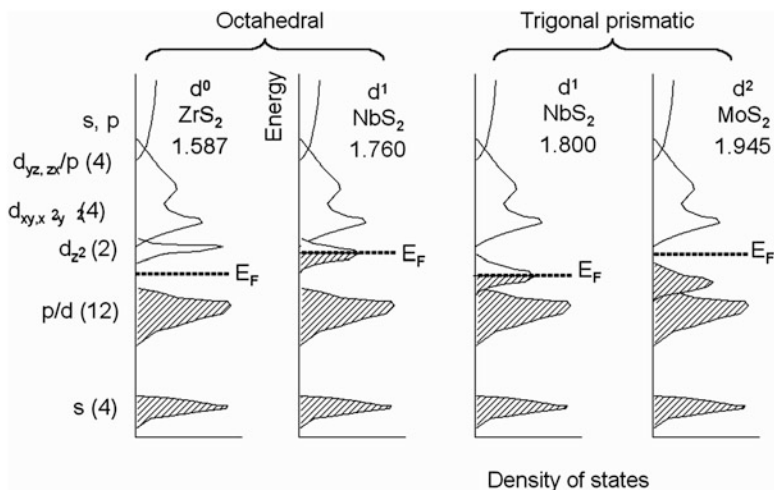


Fig. 4.5 Schematic band structures for all the TMDs compounds with octahedral and trigonal prismatic coordination. Sketches show the electronic structures before (a) and after (b) lithium intercalation with the respective position of the Fermi level

sandwich units. In the trigonal symmetry and the simplest trigonal prismatic coordination, polytypes have two sandwich repeats, and are designated 2Ha and 2Hb. The 2Ha structure is adopted by metallic group V materials such as NbS_2 and stacks the metal atoms directly above each other along the c -axis, while in the 2Hb structure, adopted by semiconducting group VI materials such as MoS_2 , the metal atoms are staggered. In the 4Hb and 6R polytypes, the coordination within successive sandwiches alternates between octahedral and trigonal prism, i.e., a mixed coordination. The six best known polytypes of transition metal dichalcogenides are shown in Fig. 4.4b. Octahedral interstitial (vacant) sites between sandwiches are represented by square sites, into which intercalation atoms may enter.

The electronic band structure of TMDs have been generally calculated using simplest molecular-orbital arguments [5] and experimentally established from the optical properties for the group IV, V, and VI TMDs. Figure 4.5 shows the schematic band structure of the MX_2 compounds having octahedral and trigonal prismatic coordination. The basic features of the band model are shown for the regular trigonal prismatic structure (groups VI and V) and the regular octahedral structure (groups IV and V). The chalcogen p states with different degrees of admixture of metal states form the main valence band, while the energy of the chalcogen s states is located 10–15 eV below. The metal d states, with possible admixture of chalcogen states, lie immediately above the p valence band, and the next higher bands are made up of metal s and p states. The d band is subdivided in accordance with the ligand field splitting. The lowest of these sub-bands can hold two electrons and is called the “ d_{z^2} ” band after Wilson and Yoffe [8]. The reason is that the d_{z^2} is split off the $d_{xy}-d_{x^2-y^2}$ band towards lower energy by the trigonal distortion. The same band-labeling scheme is used here in spite of the hybridization

between d and p states, and between the various d states. In all the compounds of the group IV to group VI transition metals, the p - and s -valence bands are completely filled, and the variations of the electrical and optical properties are largely accounted for by the gradual filling of the d_{z^2} band [12].

On the whole the band structure of an octahedrally coordinated material is characterized by greater charge transfer from the metal atom to the chalcogen atom. The p -valence band is relatively narrow (about 2.5 eV wide), while the d_{z^2} band forms part of the d band manifold which is separated from the p -valence bands by about 2 eV. This is the case for all the group IV compounds and for some of the group V compounds. The band structure of a trigonal prism coordinated material, on the other hand, has a wider p -valence band (about 5 eV wide) and there is more mixing between p and d states, while the d_{z^2} band lies close to or overlaps with the p bands and is now well separated from the rest of the d band manifold. This is the case for all the regular group VI compounds and the rest of the group V compounds.

The position of the d_{z^2} band is thus determined by the symmetry of the coordination unit. It is interesting to consider the total energy for a given coordination. This is basically determined by two competing terms: the electrostatic potential energy and the energy of the d_{z^2} electrons. In the group IV compounds, the d_{z^2} band is empty and the electrostatic energy term favors octahedral coordination, where the chalcogen atoms on two sides of the metal atoms in a sandwich are staggered, while in the group VI compounds where the d_{z^2} band is full and the bonding is predominantly covalent, it is energetically advantageous to depress the d_{z^2} band by adopting the trigonal prism coordination where the chalcogen atoms are in the eclipsed position. In the group V compounds, the d_{z^2} band is only half full, so it is not surprising that neither term necessarily dominates completely and both coordination units occur.

In the simple picture, during intercalation, the donating-electrons will occupy one of the empty d -bands. The simplest approximation to the band structure of an intercalation compound is just that of the parent host compound with the Fermi level moved up to accommodate the extra electrons.

Many techniques have been used to obtain information on the optical absorption α , the reflectivity R and dielectric constants ϵ_1 and ϵ_2 . Visible and ultra-violet absorption spectroscopy gives us the joint density of states of valence and conduction bands. Soft X-rays and synchrotron radiation give us information on conduction bands, while photoemission experiments (UPS, XPS, ESCA) can tell us about density of states in valence band and give the energies relative to the Fermi level. Typical absorption spectra for the semiconductor MoS_2 (d^2 , group VI), metal NbS_2 (d^1 , group V), and wide-band gap semiconductor ZrS_2 (d^0 , group IV) are given in Fig. 4.6. The prominent features A and B for MoS_2 are excitons, while in the metal NbS_2 one observes the characteristic free carrier absorption at about 1 eV.

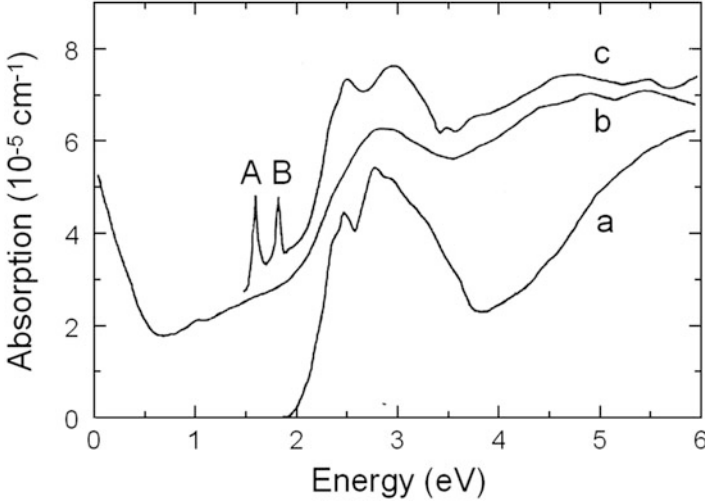


Fig. 4.6 Absorption spectra of two-dimensional TMDs: (a) 1T-ZrS₂, (b) 2H-NbS₂, and (c) 2H-MoS₂. The prominent features A and B for MoS₂ are excitonic transitions

4.4 Lithium Intercalation in TiS₂

For TMDs, the temperature dependence of the electron mobility is usually found to be much stronger than expected for acoustic phonon scattering. The resistivity for materials with a temperature independent extrinsic carrier concentration is usually fit by the empirical relation:

$$\rho = \rho_0 + AT^\alpha, \quad (4.2)$$

where ρ_0 is the temperature-independent contribution from impurity scattering and A is a constant [13]. The exponent α is found to vary from 2.3 in good-stoichiometry TiS₂ sample (with carrier concentration $n = 1.1 \times 10^{20} \text{ cm}^{-3}$) to 1.6 in poor-stoichiometry sample ($n = 2.9 \times 10^{21} \text{ cm}^{-3}$); α is found to be as large as 2.2 for ZrSe₂.

In Li_{*x*}TiS₂ the magnitude of the Hall coefficient decreases with increasing lithium content, confirming the occurrence of electron transfer from intercalates to the host [6–8]. The electron concentration in TiS₂ before intercalation is $3.1 \times 10^{20} \text{ cm}^{-3}$ indicating that this material is of stoichiometry Ti_{1.0044}S₂ [14]. Upon lithium intercalation we observe a large decrease of the resistivity as well as of the Hall coefficient. The carrier concentration in electro-intercalated samples increases to 5×10^{21} and $9.6 \times 10^{21} \text{ cm}^{-3}$ for $x = 0.25$ and 0.5 , respectively. The Hall coefficient R_H of all the samples is nearly temperature independent, as would be expected for a normal metal.

Klipstein et al. [15, 16] explain this behavior by a model involving the interplay between inter-pocket and intra-pocket scattering of electrons by longitudinal

acoustic phonons, whereby the increase in Fermi surface dimensions reduces the restriction on the wave-vector of phonons that may take part in the scattering process, implying that, as the carrier concentration increases, α should tend towards unity, which is the limit for a metal when the resistivity is solely due to a scattering of the electrons by LA-acoustic phonons. Simultaneously, the temperature T_{\min} below which the $\ln(\rho - \rho_0)$ vs. $\ln(T)$ curve starts deviating from linearity, should increase, since this deviation originates from incomplete momentum relaxation when the phonon wave-vectors characteristic of these temperatures are too short to span the Fermi surface. This model, which was originally based on studies in pristine TiS_2 with a varying degree of stoichiometry, was later verified to remain valid for higher carrier concentrations, such as in TiS_2 intercalated with lithium via the n-butyllithium technique [16] or intercalated with hydrazine [17].

Electron transfer is also apparent in the optical properties of this system. Figure 4.7 shows the absorption spectra, in the energy range 0.5–6.0 eV of pure

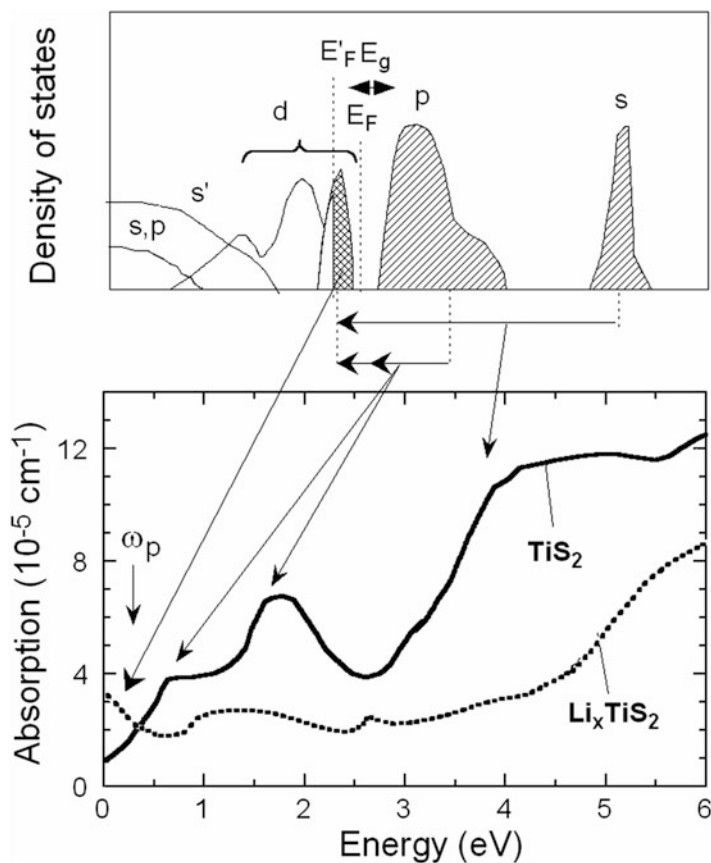


Fig. 4.7 Room-temperature absorption spectra of TiS_2 and LiTiS_2 . The schematic band structure shows that the rigid-band model may be used for the intercalation complexes

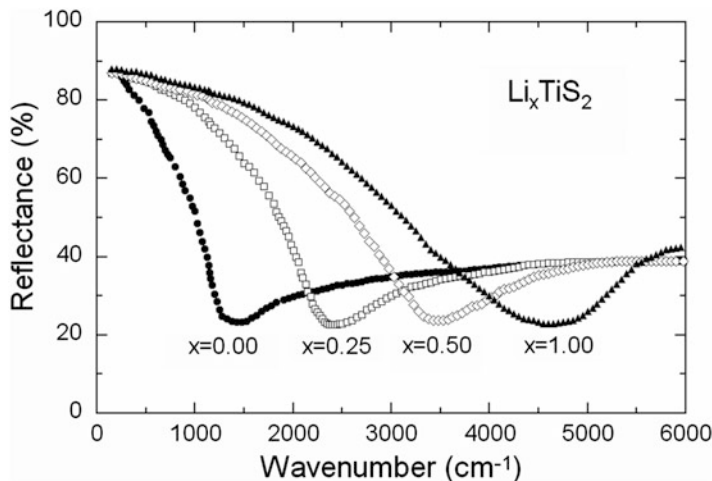


Fig. 4.8 FTIR reflectivity spectra of Li_xTiS_2 as a function of lithium content

and Li-intercalated TiS_2 [18]. In the spectrum of the intercalation complex LiTiS_2 , the free carrier absorption is evidenced below 1 eV as it is responsible for the increase of the absorption when decreasing the photon frequency in the vicinity of the plasma frequency ω_p . We also observe interband transitions which are the first direct allowed transitions from the p valence to the d conduction band at the L point of the Brillouin zone. Moving into the spectrum of Li_xTiS_2 , the onset of inter-band transitions is seen to have shifted to higher energies and the oscillator strength under the absorption band is roughly halved. Beal and Nulsen [18] argue that this is exactly what one would expect as the d_{z^2} band is now half-full following saturation of the intercalation complexes.

Another optical experiment, infrared reflectivity was carried out on Li-electro-intercalated TiS_2 [15]. Figure 4.8 shows the FTIR reflectivity spectra of Li intercalated TiS_2 single crystals as a function of $x(\text{Li})$ in the range $0 \leq x \leq 1$. We observe a large shift in the plasma edge for $\text{Li}_{1.0}\text{TiS}_2$ with respect to pure TiS_2 . According to the free-carrier Drude model (see Chap. 13), the analysis of the dielectric function gives the values as follows. In TiS_2 , the plasma edge lies around 1200 cm^{-1} , whereas in LiTiS_2 the plasma edge occurs at about 4000 cm^{-1} giving plasma frequencies of 1360 and 4100 cm^{-1} , respectively, if we take into account that the high-frequency dielectric constant remains similar to that of the pristine material and if we consider the electron effective mass as obtained by Isomaki et al. [19]. At the L-point of the Brillouin zone, Isomaki et al. estimate $m_a = 0.4 m_0$ along the a -axis. This assumption implies that the optical effective mass m_{opt} has a value higher than $1.3 m_0$. In the present studies, the Drude analysis gives a carrier concentration of $1.7 \times 10^{22} \text{ cm}^{-3}$ for complete intercalation of TiS_2 at $x = 1$. This is in excellent agreement with the theoretically expected value of $1.75 \times 10^{22} \text{ cm}^{-3}$ and very close to the value of $2.2 \times 10^{22} \text{ cm}^{-3}$ determined from Hall measurements.

We assume in the spirit of the rigid-band model [1] that intercalation changes appreciably neither the effective mass of the conduction band, nor the high-frequency dielectric constant of the host material. The charge transfer Δn from the alkali-metal atoms to the d -conduction band of the host compound can be directly calculated from the difference between ω_p^2 before and after intercalation. Here Δn is expressed in terms of the number of electrons transferred per Ti atoms. Using this method we have $\Delta n = 0.9 \pm 0.1$ electrons. The uncertainty of 0.1 electrons is thought to be a reasonable estimate in view of the assumptions made. It is interesting to note the large increase of the plasma damping factor from 310 to 2160 cm⁻¹ in Ti_{1.005}S₂ and Li_{1.0}Ti_{1.005}S₂, respectively. This increase is observed in the energy-loss function by the broadening of the plasmon peak. The damping factor can be expressed as follows:

$$\Gamma = 1/\tau = q/m^*\mu_H, \quad (4.3)$$

where μ_H is the Hall mobility of free carriers. The observed increase of Γ suggests a decrease of the Hall mobility or a modification of the effective mass in the intercalated sample. In Li_{1.0}Ti_{1.005}S₂ the electron mobility measured by Hall effect has a value of 1.9 cm²V⁻¹s⁻¹ at room temperature [14]. This value can be related with those given in the literature, namely 13.5 and 0.35 cm²V⁻¹s⁻¹ for TiS₂ and LiTiS₂, respectively [16].

The temperature dependence of the IR reflectivity spectra of the Li_{1.0}Ti_{1.005}S₂ sample is similar to those of the pure material. The spectra show a dip close to the plasma frequency $\omega_p = 4180$ cm⁻¹ extracted from analysis of the data using a Drude-like model with a frequency dependent relaxation time, as:

$$1/\tau(x, T, \omega) = x \tau_0 + \alpha \left[(pT)^2 + \omega^2 \right]. \quad (4.4)$$

A good fit to the optical data is achieved with the scattering rate given by Eq. (4.4) [20], with $p = 13.6$, against 2π in the ideal isotropic three-dimensional effective mass model [21], while the second term in ω^2 is due to the electron-electron scattering. For Li intercalated TiS₂ sample, the temperature and frequency components of Eq. (4.4) are strongly screened by the first term ($x\tau_0$) as shown in Fig. 4.9. This may be due to the complete filling of the d -band associated with a very low Hall mobility. In this case, it is difficult to evaluate the optical mobility because the quantity $\omega\tau \gg 1$ is no longer valid.

Considering that Hall measurements on the Li_{1.0}Ti_{1.005}S₂ sample give $N_H = 1.8 \times 10^{22}$ cm⁻³ and that the Fermi energy obtained by optical reflectivity measurements is $E_F = 4180$ cm⁻¹ = 0.52 eV, we may estimate the electron effective mass $m^* = 0.49 m_0$. This value is very close to the value reported for the pure material by Isomaki et al. [19]. In conclusion, it can be seen from the electrical and optical properties of the Li-intercalated TiS₂ presented above that they all can be explained in terms of the rigid-band model. It is worth mentioning here that optical absorption results by Scholz and Frindt [22] on Ag-intercalated TiS₂ also agreed with this model.

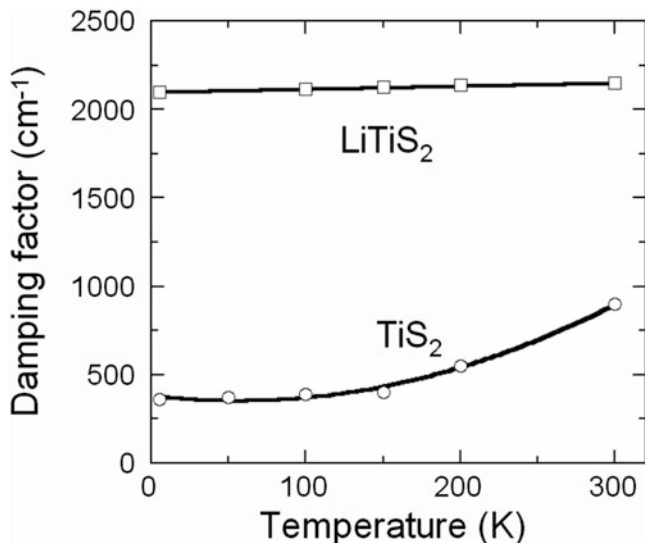


Fig. 4.9 Temperature dependence of the damping factor (inverse relaxation time) for TiS_2 and LiTiS_2

The reliability of the rigid-band model is due to the excellent structural stability of TiS_2 . From the electrochemical view point, TiS_2 was considered as the best positive electrode for lithium batteries due to its high electronic conductivity, which avoids carbon additive, and the high mobility of Li^+ ions into van der Waals planes. Unfortunately, problems came from the anode side. Note that the Li/TiS_2 electrochemical cell was invented by Broadhead and Butherus at Bell Telephone Labs, who filed their patent on 24 July 1972 [23].

4.5 Lithium Intercalation in TaS_2

Among the group-V TMDs, TaS_2 has perhaps been the subject of greatest interest, because of the fascinating structural and electronic properties that this material exhibits. Due to valence electron occupying their d_{z^2} band, this metallic compound can exist in either 1T-, 2H-, or 4H-structure [24]. As a consequence of the switching from octahedral (Oh) to trigonal prismatic (TP) coordination, the shift of the d_{z^2} band to lower energies occurs gradually. The absorption spectrum of pure 2H- TaS_2 shows a Drude edge below 1 eV associated with the free-carrier absorption in this material owing to the half-filled d_{z^2} band. After intercalation, the Drude edge disappears and the first $d_{z^2} \rightarrow d$ transition shifts toward lower energy. These changes are attributed to the gradual filling of the d_{z^2} band by electron transferred from lithium.

The absorption spectrum of 1T- TaS_2 is shown in Fig. 4.10. Near 1.5 eV, the absorption bands are associated with the $d_{z^2_1} \rightarrow d_{z^2_2}$ and $d_{z^2_1} \rightarrow d$ transitions,

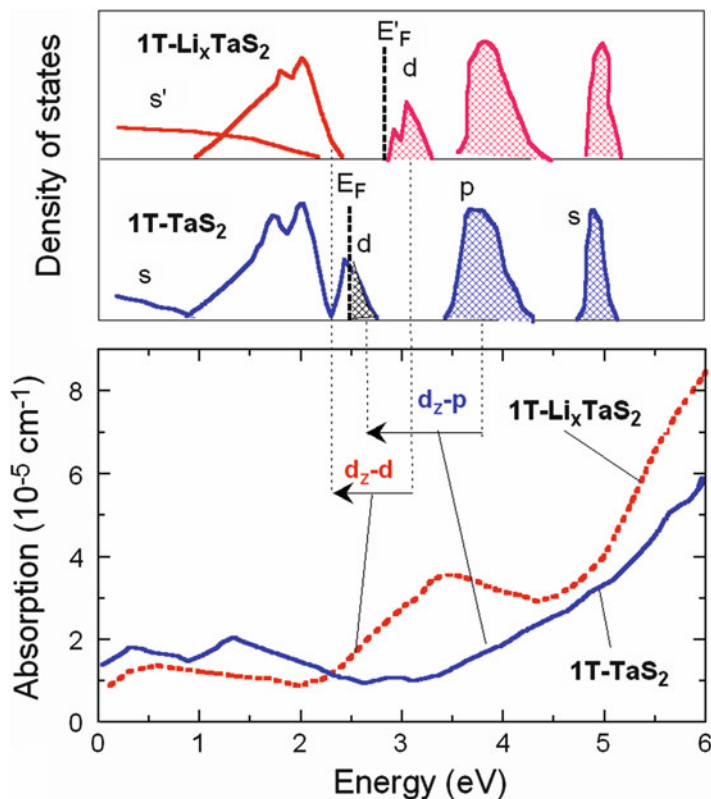


Fig. 4.10 Absorption spectra of pure 1T-TaS₂ and 1T-Li_xTaS₂. The schematic band structure shows the lowering of the d_z band upon Li intercalation. Reproduced with permission from [24]. Copyright 1986 Kluwer Academic Press

whereas the band above ~ 3.5 eV owing to $p \rightarrow d_{z^2}$ transition. Charge transfer from Li to the host lattice increases the population of the d_{z^2} band and raises the Fermi level E_F to a new energy, E_F' . The displacement of the strong absorption edge around ~ 3 eV indicates a considerable lowering of the d_{z^2} band with respect to its position in the pristine material. The lowering of the d_{z^2} band is attributed to the filling with electrons donated by Li, as well as the modification of the crystal structure that is an increase of the c/a ratio after intercalation [25]. These results provide further support to the argument that, upon lithium intercalation the rigid-band model is not entirely applicable in 1T-TaS₂.

4.6 Lithium Intercalation in 2H-MoS₂

Among the group-VI TMDs, MoS₂ is one of the materials where intercalation reactions induce a transition of the host related to local ligand field modification. In this particular case, molybdenum presents a trigonal prismatic sulfur

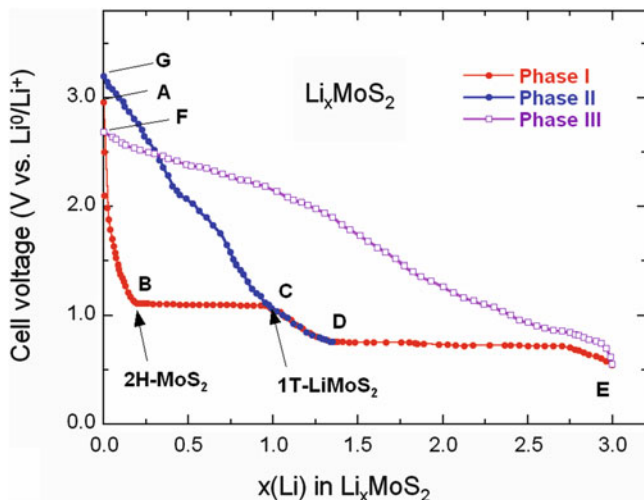


Fig. 4.11 Electrochemical profile of the Li-MoS₂ system as a function of the Li content in Li_xMoS₂. Reproduced with permission from [29]. Copyright 2002 Elsevier

coordination that changes the octahedral one (TP → Oh transition) [26–28]. The structure modification is accompanied by an increase of the *M*-*X* band ionicity in agreement with the respective stability of the new atomic arrangement, the Coulomb repulsion between partially charged ligands favoring the octahedral form. Also, the comparison of the *d*-band density of states of 2H-MoS₂ and hypothetical 1T-LiMoS₂ shows that the occupied bands, which contain six states, are lower in the case of the Oh phase. This effect corresponds to the glide process between Mo and S atoms. This is a fine example of destabilization through lithium reduction.

Figure 4.11 shows the voltage profile vs. composition *x*(Li) of the Li//Li_xMoS₂ cell using 1 mol L⁻¹ LiClO₄ in propylene carbonate as electrolyte [29]. The Li-MoS₂ system exhibit three distinct phases in good agreement with the work of Hearing et al. [30]. The discharge reaction of a fresh cell occurs in the range 3.0–0.55 V with two voltage plateaus at 1.1 and ~0.7 V when 3Li are intercalated in the layered MoS₂ lattice. The first discharge curve (phase I) exhibits a plateau in the range 0.25 ≤ *x* ≤ 1 that corresponds to a two-phase system including both 2H-Li_{0.25}MoS₂ and 1T-LiMoS₂ structures. For *x* = 1 the complete transformation from (TP) to (Oh) coordination is attributed to a process, which is driven by a lowering of the electronic energy for the octahedral structure when electrons are donated from Li to the MoS₂ layer upon intercalation. The octahedral transformation starting at *x* ≈ 0.25 completes around *x* = 1.0 and is not preserved on subsequent cycling [1, 26, 27]. For *x* > 1, the phase II is formed, which appears to be reversible in the range 0.75–3.2 V without plateau formation. This phase II is a preferred phase (path D-G in Fig. 4.11) for battery use that requires the so-called battery formation process, i.e., first discharge down to 0.75 V. The phase III (path E-F) occurs at the end of the second plateau. This phase is not suitable because of the poor reversibility [30].

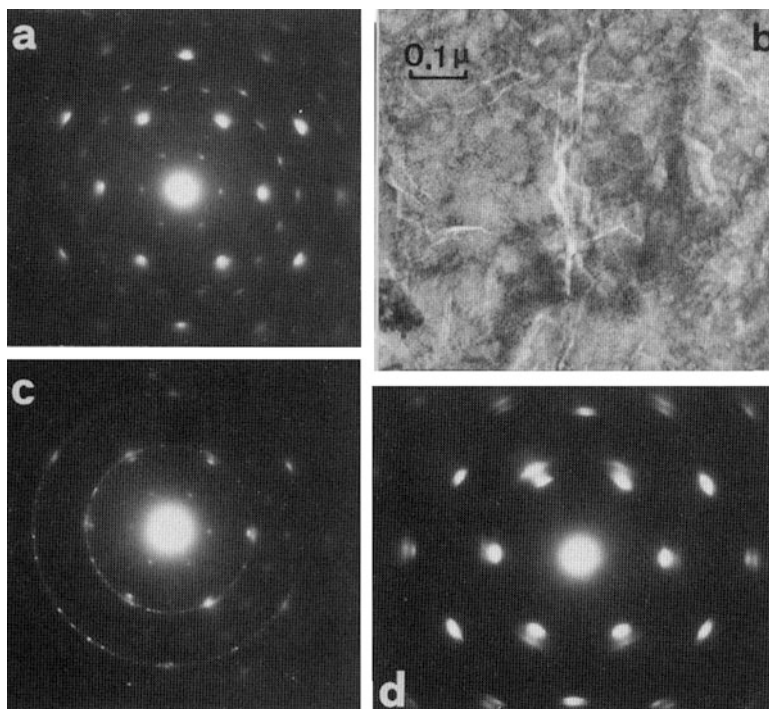


Fig. 4.12 Li intercalation of MoS₂ in n-butyllithium. (a) After 10 min, defects are created near the edges and in the steps of the specimen denoted by *arrows*. (b) After 2 h intercalation, superlattice spots appear (denoted by the letter *s*), which are indexed as (1/201/20). Notice also the splitting of the main spots (denoted by the letter *M*). (c) A micrograph taken from the same area reveals that the specimen is heavily defected owing to intercalation. (d) Distribution of lithium vs. Distance from the edges of the specimen as revealed by SSNTD images. Reproduced with permission from [29]. Copyright 2002 Elsevier

Electron diffraction studies on the Li-MoS₂ system have shown that the structural transformation is accompanied by a $2a_0 \times 2a_0$ superlattice formation observed for the composition $x \approx 0.25$, which is interpreted as a pseudo-staging on the basal hexagonal lattice (Fig. 4.12) [31]. This superlattice formation was also observed in the incremental capacity dQ/dV obtained from electrochemical measurements [28] and in the Raman scattering spectra of Li_{0.3}MoS₂ [32, 33]. However, we do expect that the lithiation process is accompanied by the raising of the Fermi level due to the charge transfer from Li intercalation. This is depicted in Fig. 4.13, where the temperature dependence of the electrical conductivity of lithium intercalated MoS₂. Undoped MoS₂ is a n-type semiconductor with $\sigma \sim \exp(-E_a/k_B T)$, where $E_a = 0.05$ eV, and Li_{0.3}MoS₂ is a highly degenerate semiconductor with $\sigma \sim T^{-1.4}$. Here, we must be aware of the limitations of the rigid band model. It is probably non appropriate for Li_{*x*}MoS₂ because the fully occupied d_{z^2} states in the pristine material imply new electrons to enter the next higher d band with a change of the c/a ratio associated with the destabilization of the host lattice.

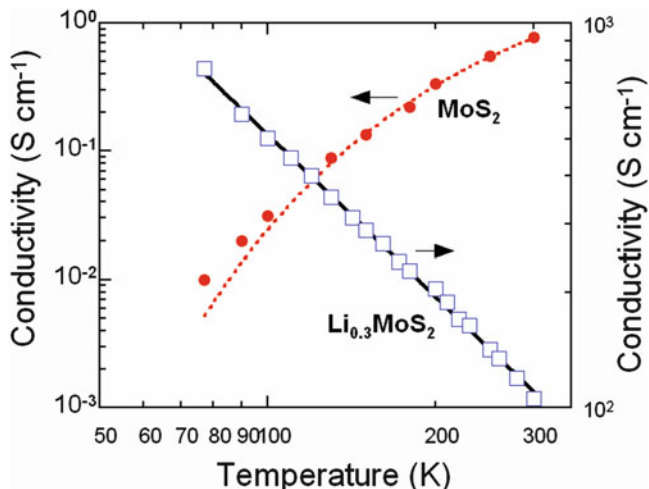


Fig. 4.13 Temperature dependence of the electrical conductivity of lithium intercalated MoS₂. Reproduced with permission from [29]. Copyright 2002 Elsevier

Following the above structural transformation, phonon spectroscopy offers an excellent way of quantifying the degree of anisotropy not only by distinguishing between inter- and intra-layer normal modes but also by determining the shear moduli in different directions. The Raman spectrum of 2H-MoS₂ at room temperature is shown in Fig. 4.14. It exhibits four Raman-active bands that are the intra-layer A_{1g} mode at 407 cm^{-1} involving motion along the c -axis, the intra-layer E_{2g} mode at 382 cm^{-1} involving motion in the based plane, the E_{1g} mode at 286 cm^{-1} and the rigid-layer (RL) mode at 32 cm^{-1} of E_{2g} symmetry. This last mode is of interlayer type involving rigid motion of neighboring sandwiches in opposite phase.

The Raman spectra of Li_xMoS_2 with $x \approx 0.1$ and $x = 0.3$ (Fig. 4.14) display the structural changes from the β -phase (2H structure) to a α -phase (1T structure) upon Li intercalation [32]. This transformation from trigonal prismatic to octahedral coordination has been attributed to a process which is driven by a lowering of the electronic energy for the octahedral structure when electrons are donated from Li to the MoS₂ layer during intercalation [33]. The octahedral transformation in Li_xMoS_2 starts at $x = 0.1$ and completes around $x = 1$. For a degree of intercalation $x \approx 0.1$, the Raman intensity is considerably reduced (by a factor 5) and we observe two new bands: a broad peak located at 153 cm^{-1} (A-line) and a weak peak situated at 205 cm^{-1} (B-line) and the intensity of the RL mode is reduced. The two pristine intra-layer modes can still be observed, with little shift in frequency, but both of them are split to give weak additional side bands towards lower energies (C- and D-line). These bands are attributed to the Davydov pairs of the optical phonon branches. For $x = 0.3$, the spectrum of Li_xMoS_2 is modified with respect to the former ones. The RL mode is no longer recorded. All the other lines are still observed. In addition, a small shift in frequency of the lattice modes of MoS₂ can be observed [33].

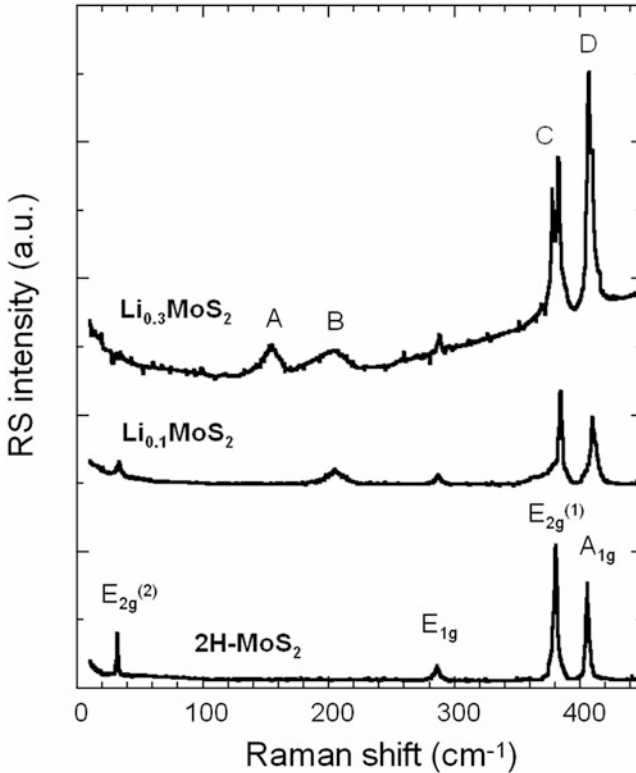


Fig. 4.14 Raman spectra of 2H-MoS₂ natural crystal as a function of Li content lithium

A simple model has been used to calculate the frequencies of the new modes appearing after Li intercalation. The intercalation mode is given by:

$$\omega_{\text{int}}(0) = [k(2m_1 + m_2)/m_1m_2]^{1/2}, \quad (4.5)$$

where m_1 and m_2 are the masses of the MoS₂ molecule and of the Li atom, respectively, and k is the force constant between the S and Li atoms. We estimate $k = 8.23 \times 10^3 \text{ dyn cm}^{-1}$, which is much smaller than the intra-layer force constants. For a degree of intercalation $x = 0.3$, we assume that Li_{0.3}MoS₂ is a two-phase system. The following changes on the lattice dynamics can be expected. The RL mode disappears because the elementary cell of the 1T-structure contains only one molecular unit (3 atoms per sandwich). The symmetry changes from D_{6h} to D_{3d} and the new symmetry allows only the two Raman active A_{1g} and E_g modes representative of the intra-layer atomic motions. The weak spacing expansion observed upon Li intercalation and the difference of the molybdenum coordination do not modify significantly the frequency of these modes. A simplest calculation gives a change of about 6 % in frequency. Thus, we can trust the validity of the lattice dynamics model using a 2H-structure [33]. Finally, it is obvious that Li intercalation into molybdenum disulfides does not satisfy the concept of rigid-band model.

4.7 Lithium Intercalation in WS₂

Among the TMDs materials, WS₂, which belongs to the group VIb transition metal, crystallizes into a layered structure identical to MoS₂. Two polytypes hexagonal (2H) and rhombohedral (3R) are commonly found among the materials with trigonal-prismatic coordination. Varieties of other polymorphic structures have been described such as o-WS₂ and 2M-WS₂ [34]. Orthorhombic β-WS₂ (1T-structure) has been prepared by removing Na from Na_xWS₂ [35]. WS₂ is a grey-black indirect-gap semiconductor with a n-type character and an energy gap of 1.35 eV due to electronic transition of the $d \rightarrow d$ type. In terms of the two-dimensional WS₂ band structure direct low energy transitions at about 1.9–2.5 eV are characterized by A and B exciton pairs and its narrow d_{z^2} subband is completely filled. The conduction band based on $d_{x^2-y^2}$, d_{xy} orbitals is empty and can thus be populated by electron donors. The observation by Rüdorff [36] that WS₂ forms metal intercalated products when the dichalcogenide is treated with liquid ammonia solutions of alkali metals prompted us to examine more generally the features of electrochemically Li-intercalated WS₂. Somoano et al. [37] have also shown that intercalation compounds are found in the case of tungsten derivatives. Omloo and Jellinek [38] made an attempt to understand the instability of WS₂ and WSe₂ intercalated by alkali metals and alkaline earths. The electrochemical features of the intercalation-deintercalation reaction of Li_xWS₂ is shown in Fig. 4.15a [39]. The voltage-composition curve displays features as follows: (a) the initial OCV of 3.0 V, (b) the emf decreases smoothly from 3.0 to 2.2 V in the range $0 \leq x \leq 0.2$ and a break is clearly observed at about $x=0.2$, (c) for $x > 0.2$ the discharge curve occurs with a pseudo-plateau at about 2.1 V, (d) the cell voltage drops to 0.5 V for $x=0.6$ giving a specific energy density of 140 Wh kg⁻¹. The incremental capacity $-(\partial x/\partial V)$ curve recorded at the first discharge (Fig. 4.15b) shows patterns comparable to a double-site energy system [40]. This should be the evidence of either increasing repulsive forces between inserted ions or formation of a new phase. During the insertion process the alkali metal transfers electron to the

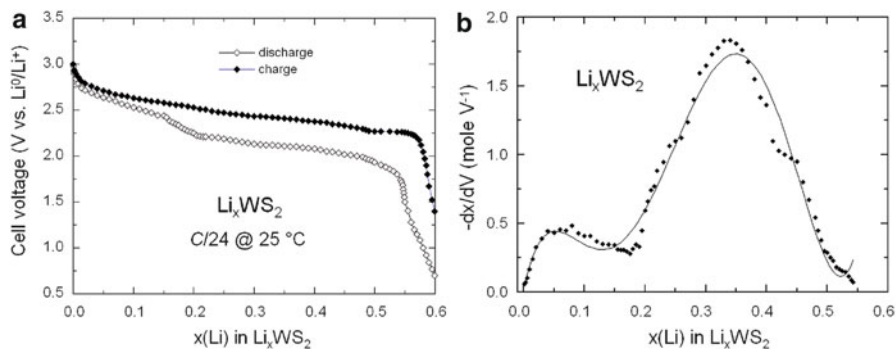


Fig. 4.15 (a) Discharge–charge curves of an electrochemical Li//WS₂ cell using the 3R-WS₂ polymorph as cathode material. (b) Incremental capacity dx/dV vs. composition

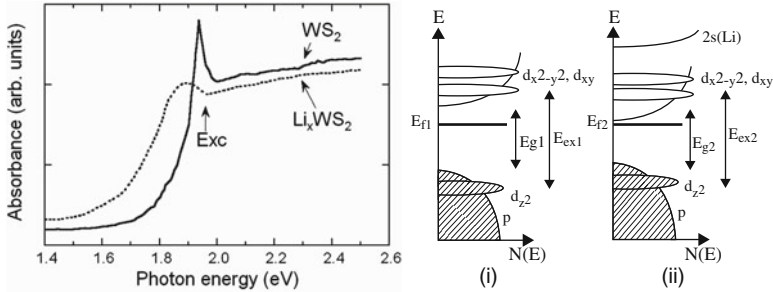


Fig. 4.16 (Left) The absorbance spectra recorded at 5 K of pure WS₂ and Li-intercalated WS₂ single crystal containing a small amount of lithium $x=0.1$. (Right) Electronic band structure of trigonal prismatic dichalcogenide (i) pure WS₂ and (ii) Li_{0.1}WS₂

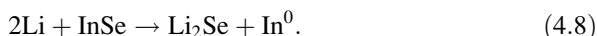
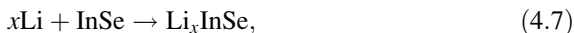
empty conduction band based on $d_{x^2-y^2}$, d_{xy} orbitals of W. Intercalation with electron donors is expected to populate these higher energy bands and give metallic properties. According to molecular-orbital calculations [25] with the d_{z^2} band already full and intercalation increasing the d band population from d^2 to d^3 , the electron energy can be lowered by a trigonal. Indeed, for the W layered compounds, the number of d electrons exceeds d^2 during intercalation. The stability of intercalates of WS₂ is clearly related to the ionization potentials of the inserted metals and the affinity of the layer compound [38] and the prismatic coordination is destabilized on addition of lithium ions for $x > 0.2$. It was suggested that the result is a structural transformation from 3R-WS₂ to 2H-Li_xWS₂ due to the instabilities in the interlayer structure. Later in the discussion it will be demonstrated that upon Li⁺ insertion the interlayer spacing increases with a small expansion [41].

Figure 4.16a shows the absorbance spectra recorded at 5 K of pristine WS₂ and Li_{0.1}WS₂ samples in the energy range 1.4–2.5 eV. In these spectra, we observe absorption edge at 1.9 and 1.7 eV and side-band at 1.93 and 1.88 eV corresponding to the absorption edge and the excitonic peak of WS₂ and Li_{0.1}WS₂, respectively. The exciton transition at about 1.93 eV is attributed to the smallest direct gap at K (the zone-edge point in the (110) direction) in between the d_{z^2} valence states and the $d_{x^2-y^2}$, d_{xy} conduction states, split by interlayer interactions and spin-orbit coupling [42]. Upon Li intercalation, modifications in the absorption spectrum are observed, with a red shift of absorption edge and the vanishing of the exciton peak (located at E_{ex} on the curves) due to free carrier screening. In this process the free carriers arise from band filling above the full d_{z^2} band. For Li_xWS₂ the donated electrons should go into the empty conduction band based on the $d_{x^2-y^2}$, d_{xy} orbitals. The half width at half-maximum (HWHM) of the exciton of pure WS₂ at 5 K is about 20 meV, whereas one observes a HWHM of 55 meV for Li_xWS₂. The primary phenomenon associated with the lithium intercalation in WS₂ is the donation of x electrons from the guest to the host matrix. The second effect is that the interband absorption edge around 1.9 eV shifts to lower energies with Li insertion (Fig. 4.16b). This result can be understood in terms of a destabilization of the electronic band structure. The shift of the fundamental absorption edge toward lower energies can be attributed to

an interaction between the conduction band made up of s and p orbitals and the $2s$ orbitals of lithium. Thus, the net effect is a decrease of the optical band gap of about 0.22 eV. Optical effects in Li-intercalated WS_2 can be satisfactorily interpreted in terms of electron donation but the rigid-band model is essentially inadequate in such a compound. One may note that, in the studied energy range (1.4–2.5 eV), intercalation of Li ions did not give rise to extra absorption bands [42].

4.8 Lithium Intercalation in InSe

The intercalation of lithium in InSe has been extensively studied. Indium monoselenide is a layered semiconductor in which each layer consists of four close-packed, covalently bounded, monoatomic sheets in the sequence Se-In-In-Se. When material is grown by the Bridgman method, the 3R polytype (γ -InSe) crystallizes in a rhombohedral system with the R3m space group (C_{3v}^5) with the primitive unit cell containing three layers but only one molecule [43, 44]. The layers are stacked in the sequence $CBA\Box ABC$ separated by weak interlayer interaction (often referred to as van der Waals-like). The square symbol represents the empty site available for insertion. The interaction of cleaved InSe crystals with lithium was investigated by electrochemical titration, in situ X-ray diffractometry, and by X-ray photoemission spectroscopy showing a competition between intercalation and chemical decomposition reactions expressed as [45–47]:



The effect of Li insertion on the electronic structure of InSe has been evidenced by photoluminescence, Raman scattering, and absorption measurements [48, 49]. Upon lithium insertion, one observes different features in the optical spectra of Li_xInSe , which appear to be strongly dependent on the Li concentration. For $x \approx 0.1$, a blue shift of the fundamental absorption threshold is due to the destabilization of both the highest valence band and the lowest conduction band. This is attributed to the (s, p_z) character of these energy states which interact with the lithium s -orbital. New broad bands appeared at 1.278 and 1.206 eV in the photoluminescence spectrum of $\text{Li}_{0.1}\text{InSe}$, which were attributed to transitions associated with the lattice deformations introduced by the expansion perpendicular to the basal plane and to those associated with the lithium donor levels, respectively [49].

Figure 4.17 displays the evolution of Raman spectra of Li_xInSe . The structural modification due to lithium insertion is clearly shown from these experiments. The vibrational feature of γ -InSe (C_{3v}^5 symmetry) includes six Raman-active modes such as $3A_1 + 3E$ [50]. The Raman spectrum displays a low-frequency band at 41 cm^{-1} (E species), a strong band at 117 cm^{-1} (A_1 species), three bands located in the polar phonon domain at 177, 199, and 211 cm^{-1} (LO and TO modes), and a

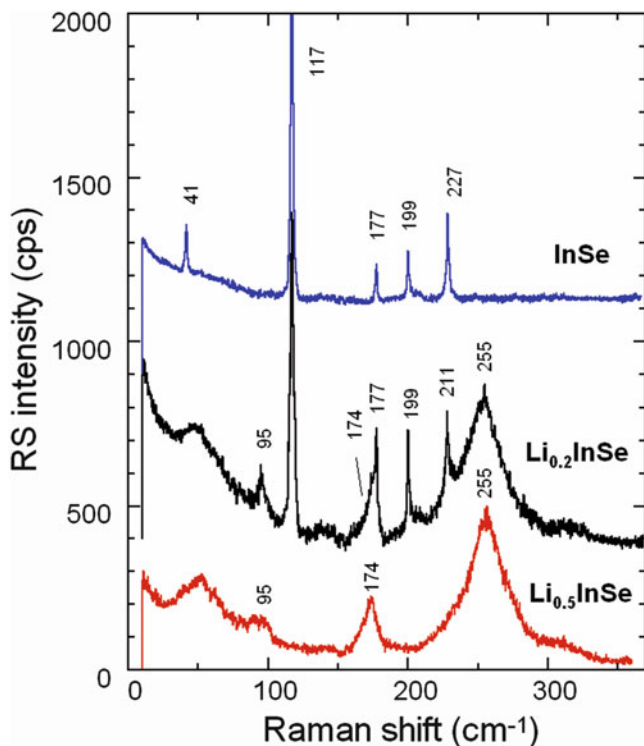


Fig. 4.17 Raman scattering spectra of pristine and Li intercalated γ -InSe single crystal. The intercalated samples were prepared by galvanostatic method in lithium cell

nonpolar mode at 225 cm^{-1} (A_1 species). After intercalation ($x \approx 0.2$), the Raman spectrum is drastically modified. It displays vanishing bands of the pristine material and additional broad peaks centered at 95 , 174 and 257 cm^{-1} . These bands, which are attributed to the presence of Li_2Se and amorphous Se in the host lattice, respectively, dominate the RS spectrum for $x = 0.5$. Here, the bending mode, $\nu(\text{Se-Li-Se})$, appears at 174 cm^{-1} in Li_xInSe . At this stage, the crystal is partially decomposed in the presence of Li producing Li_2Se , amorphous Se and In metal. At this stage, we explain these experimental data by the simple schematic band structure presented in Fig. 4.18. At relatively low lithium concentration ($x \approx 0.1$), we assume the picture (Fig. 4.18a) where the principal electronic states are grouped into two categories (s, p_z) and (p_x, p_y). The electronic lithium-like s -orbital, which is located at the higher position energy into the conduction band, repulses the lower levels of same symmetry (Fig. 4.18b). The effect of Li intercalation on the interband optical transitions is rather weak but nevertheless clearly observable [52]. These results suggesting a decomposition process are in good accordance with the potential-composition curve (not shown) in which the plateau represents

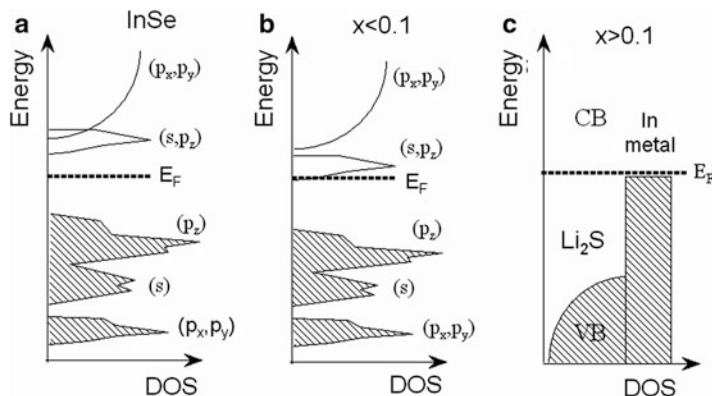


Fig. 4.18 Schematic representation of the electronic band structure evolution of InSe upon Li insertion. (a) pristine material, (b) Li_xInSe for $x \leq 0.1$, and (c) Li_xInSe for $x \geq 0.1$ showing the chemical decomposition

the Gibbs free energy $\Delta G_{\text{react}} = -140 \text{ kJ mol}^{-1}$ for the decomposition reaction of InSe by Li. This means for $x > 0.1$, a chemical decomposition of InSe occurs with two competitive reactions given by Eqs. (4.1) and (4.2).

4.9 Electrochemical Properties of TMCs

Figure 4.19 compares the discharge profile of prior nonaqueous rechargeable lithium batteries including lithium metal as anode, $1 \text{ mol L}^{-1} \text{ LiClO}_2$ in propylene carbonate (PC) as electrolyte and MX_2 dichalcogenide as cathode. Such positive electrodes have several advantages: (1) they deliver high voltage, (2) water hydrogen is not liberated by electrolytic reduction, (3) materials exhibit high conductivity, and (4) these electrodes are insoluble in electrolyte solvents such as PC [51]. Note that PC cannot be used with graphitic carbon as negative electrode, but we consider in this chapter only half-cells, i.e., lithium metal is the negative electrode. The change of the cell voltage depends in general on the electronic states of the material. During the runaway, the voltage is also a function of the electrode composition x , which represents the fraction of electrons in the $\text{Li}_x\langle H \rangle$ host. Also, Li–Li interactions play a role in determining the magnitude of the voltage. It is therefore instructive to analyze the dependence of the voltage, V vs. x . Operating voltage of a solid-state redox reaction associated with lithium ions insertion or extraction usually exhibits subtle dependence on the concentration of lithium ions and electrons in a solid matrix, which does not follow the simple Nernst equation. Problems that have limited the usefulness of these batteries are associated to the dendritic growth which eventually generate short circuit between the negative and the positive electrodes.

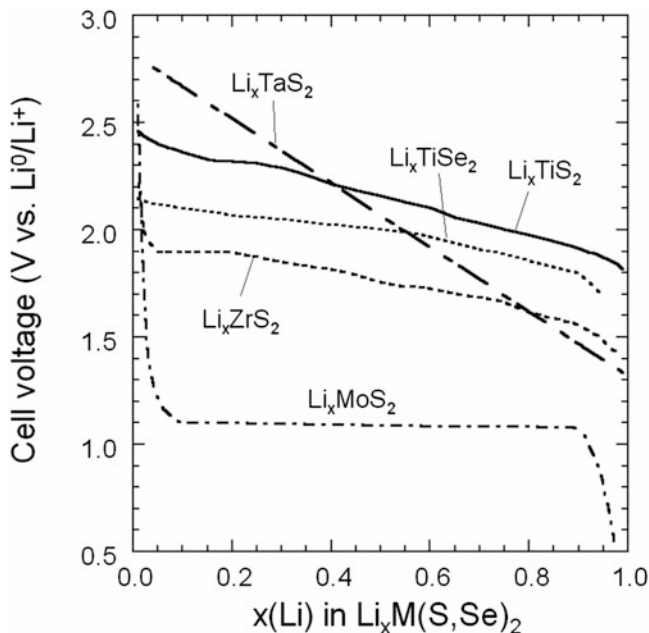


Fig. 4.19 Discharge voltage curves of the Li intercalation reaction into several TMD frameworks

4.10 Concluding Remarks

In this chapter we have shown that intercalation is a heterogeneous process in layered materials. Consequently, the rigid-band model leaving the electronic band structure of the host mostly unchanged can only be rarely applied. The electronic band structure of transition-metal dichalcogenides of group IV with the octahedral coordination in their $X-M-X$ sandwich is not really affected by the lithium intercalation. There are two main energy terms to be considered in relation to the stability of a given coordination structure. These are the lattice energy term on the one hand which is based on ionicity and the Coulomb interactions between ions (the Madelung energy), and the electronic band energy term on the other, which depends on the energy position of the filled bands, particularly that of the occupied d_{z^2} band (the lowest lying d sub-band of the d -band manifold).

The striking example is the reactivity of lithium with III-VI layered compounds such as the decomposition of Li intercalated InSe with the formation of lithium selenide, Li_2Se , observed by Raman spectroscopy on specimens prepared by various intercalation methods. The insertion of Li into MoS_2 appears more stable with the occurrence of a superlattice formation at $x(\text{Li}) \approx 0.25$ but a structural transformation from 2H-MoS_2 (β -phase) to 1T-MoS_2 (α -phase) occurs for $x \approx 1$. This process is irreversible but the intercalation-deintercalation reaction is possible with the 1T-MoS_2 , which could act as a positive electrode in rechargeable lithium batteries after formation of the cells.

References

1. Liang WY (1989) Electronic properties of intercalation compounds. *Mater Sci Eng B* 3:139–143
2. Wilson JA (1977) Concerning the semimetallic characters of TiS_2 and TiSe_2 . *Solid State Commun* 22:551–553
3. Laubach S, Schmidt PC, Ensling D, Schmid S, Jaegermann W, Thisen A, Nikolowski K, Ehrenberg H (2009) Changes in the crystal and electronic structure of LiCoO_2 and LiNiO_2 upon Li intercalation and de-intercalation. *Phys Chem Chem Phys* 11:3278–3289
4. Sellmyer DJ (1978) Electronic structure of metallic compounds and alloys. *Solid State Phys* 33:83–248
5. Jones H (1934) The theory of alloys in the γ -phase. *Proc R Soc London Ser A* 144:225–234
6. Friedel J (1954) Electronic structure of primary solid solutions in metals. *Adv Phys* 3:446–507
7. Goodenough JB, Kim Y (2010) Challenges for rechargeable Li batteries. *Chem Mater* 22:587–603
8. Wilson JA, Yoffe AD (1969) The transition metal dichalcogenides discussion and interpretation of the observed optical, electrical and structural properties. *Adv Phys* 18:193–335
9. Huisman R, de Jong R, Haas C (1971) Trigonal-prismatic coordination in solid compounds of transition metals. *J Solid State Chem* 3:56–66
10. Williams PM (1976) Photoemission studies of materials with layered structures. In: Lee PA (ed) *Physics and chemistry of materials with layered structure*, vol 4. Reidel, Dordrecht, pp 273–341
11. Brown BE, Beerntsen DJ (1965) Layer structure polytypism among niobium and tantalum selenides. *Acta Crystallogr* 18:31–36
12. Hibma TJ (1982) Structural aspects of monovalent cation intercalates of layered dichalcogenides. In: Whittingham MS, Jacobson AJ (eds) *Intercalation chemistry*. Academic, New York, pp 285–313
13. Julien C, Balkanski M (1993) Is the rigid band model applicable in lithium intercalation compounds? *Mater Res Soc Symp Proc* 293:27–37
14. Julien C, Samaras I, Gorochov O, Ghorayeb AM (1992) Optical and electrical-transport studies on lithium-intercalated TiS_2 . *Phys Rev B* 45:13390–13395
15. Klipstein PC, Pereira CM, Friend RH (1984) Transport and Raman investigation of the group IV layered compounds and their lithium intercalates. In: Acrivos JV, Mott NF, Yoffe AD (eds) *Physics and chemistry of electrons and ions in condensed matter*, NATO-ASI Series, Ser. C 130. Reidel, Dordrecht, pp 549–559
16. Klipstein PC, Friend RH (1987) Transport properties of Li_xTiS_2 ($0 < x < 1$): a metal with a tunable Fermi level. *J Phys C* 20:4169–4180
17. Ghorayeb AM, Friend RH (1987) Transport and optical properties of the hydrazine intercalation complexes of TiS_2 , TiSe_2 and ZrS_2 . *J Phys C* 20:4181–4200
18. Beal AR, Nulsen S (1981) Transmission spectra of lithium intercalation complexes of some layered transition-metal dichalcogenides. *Phil Mag B* 43:965–983
19. Isomaki H, von Boehm J, Krusius P (1979) Band structure of group IVA transition-metal dichalcogenides. *J Phys C* 12:3239–3252
20. Julien C, Ruvalds J, Virosztek A, Gorochov O (1991) Fermi liquid reflectivity of TiS_2 . *Solid State Commun* 79:875–878
21. Virosztek A, Ruvalds J (1990) Nested-Fermi-liquid theory. *Phys Rev B* 42:4064–4072
22. Scholz GA, Frindt RF (1983) Transmission spectra of silver intercalated 2H-TaS_2 and 1T-TiS_2 . *Can J Phys* 61:965–970
23. Broadhead J, Butherus AD (1972) Rechargeable nonaqueous battery. US Patent 3,791,867, Accessed 12 Feb 1974
24. Ghorayeb AM, Liang WY, Yoffe AD (1986) Band structure changes upon lithium intercalation. In: Dresselhaus MS (ed) *Intercalation in layered compounds*, NATO-ASI Series, Ser B 148. Plenum, New York, pp 135–138

25. Liang WY (1986) Electronic properties of transition metal dichalcogenides and their intercalation complexes. In: Dresselhaus MS (ed) *Intercalation in layered compounds*, NATO-ASI Series, Ser. B 148. Plenum, New York, pp 31–73
26. Py MA, Haering RR (1983) Structural destabilization induced by lithium intercalation in MoS_2 and related compounds. *Can J Phys* 61:76–84
27. Selwyn LS, McKinnon WR, von Sacken U, Jones CA (1987) Lithium electrochemical cells at low voltage. Decomposition of Mo and W dichalcogenides. *Solid State Ionics* 22:337–344
28. Samaras I, Saikh I, Julien C, Balkanski M (1989) Lithium insertion in layered materials as battery cathodes. *Mater Sci Eng B* 3:209–214
29. Julien CM (2002) Lithium intercalated compounds: charge transfer and related properties. *Mater Sci Eng R* 40:47–102
30. Hearing RR, Stiles JAR, Brandt Klaus (1979) Lithium molybdenum disulphide battery cathode. US Patent 4,224,390, Accessed 23 Sep 1980
31. Chrissafis K, Zamani M, Kambas K, Stoemenos J, Economou NA, Samaras I, Julien C (1989) Structural studies of MoS_2 intercalated by lithium. *Mater Sci Eng B* 3:145–151
32. Sekine T, Julien C, Samaras I, Jouanne M, Balkanski M (1989) Vibrational modifications on lithium intercalation in MoS_2 . *Mater Sci Eng B* 3:153–158
33. Julien C, Sekine T, Balkanski M (1991) Lattice dynamics of lithium intercalated MoS_2 . *Solid State Ionics* 48:225–229
34. Mattheis LF (1973) Band structure of transition-metal-dichalcogenide layer compounds. *Phys Rev B* 8:3719–3740
35. Tsai HL, Heising J, Schindler JL, Kannewurf CT, Kanatzidis MG (1997) Exfoliated-restacked phase of WS_2 . *Chem Mater* 9:879–882
36. Rüdorff W (1966) Reaktionen stark elktropositiver metalle mit graphit und mit metallidichalcogeniden. *Angew Chem* 78:948
37. Somoano RB, Hadek V, Rembaum A (1973) Alkali metal intercalates of molybdenum disulphide. *J Chem Phys* 58:697–701
38. Omloo WPF, Jellinek F (1970) Intercalation compounds of alkali metals with niobium and tantalum dichalcogenides. *J Less Common Metals* 20:121–129
39. Julien C, Yebka B (1996) Studies of lithium intercalation in 3R-WS_2 . *Solid State Ionics* 90:141–149
40. DiSalvo FJ, Bagley BG, Voorhoeve JM, Waszczak JV (1973) Preparation and properties of a new polytype of tantalum disulfide (4Hb-TaS_2). *J Phys Chem Solids* 34:1357–1362
41. Julien C (1990) Technological applications of solid state ionics. *Mater Sci Eng B* 6:9–28
42. Julien C, Yebka B, Porte C (1998) Effects of the lithium intercalation on the optical band edge of WS_2 . *Solid State Ionics* 110:29–34
43. Likforman A, Carre D, Etienne J, Bachet B (1975) Structure cristalline du monoséléniure d'indium InSe. *Acta Crystallogr B* 31:1252–1254
44. Ikari T, Shigetomi S, Hashimoto K (1982) Crystal structure and Raman spectra of InSe. *Phys Status Sol (b)* 111:477–481
45. Levy-Clement C, Rioux J, Dahn JR, McKinnon WR (1984) In-situ X-ray characterization of the reaction of lithium with InSe. *Mater Res Bull* 19:1629–1634
46. Schellenberger A, Lehman J, Pettenkofer C, Jaegermann W (1994) Electronic structure of in-situ (in UHV) prepared Li/InSe insertion compounds. *Solid State Ionics* 74:255–262
47. Schellenberger A, Jaegermann W, Pettenkofer C, Tamm Y (1995) Electronic structure and electrochemical potential of electrons during alkali intercalation in layered materials. *Ionics* 1:115–124
48. Julien C, Jouanne M, Burret PA, Balkanski M (1989) Effects of lithium intercalation on the optical properties of InSe. *Mater Sci Eng B* 3:39–44
49. Burret PA, Jouanne M, Julien C (1989) Theoretical calculations and Raman spectrum of intercalation modes in Li_xInSe . *Z Phys B Condensed Matter* 76:451–455
50. Kuroda N, Nishina Y (1978) Resonant Raman scattering at higher M_0 exciton edge in layer compound InSe. *Solid State Commun* 28:439–443
51. Julien C, Nazri GA (2001) Intercalation compounds for advanced lithium batteries. In: Nalwa HS (ed) *Handbook of advanced electronic and photonic materials*, vol 10. Academic Press, San Diego, pp 99–184